Showcasing research from Professors Voïtchovsky and Kusumaatmaja's laboratories, Department of Physics, Durham University, and School of Engineering, Edinburgh University, UK.

Nanoparticle adhesion at liquid interfaces

Nanoparticle adhesion at liquid interfaces is ubiquitous in nature and plays an important role in numerous technological applications. A combination of atomic force microscopy measurements and modelling quantifies the force needed to remove nanoparticles from the interfaces as a function of their chemistry and shape.

As featured in:

ROYAL SOCIETY OF CHEMISTRY

rsc.li/soft-matter-journal

Check for updates

Nanoparticle adhesion at liquid interfaces†

Ke Sun, [ID] [a] Yonas Gizaw,[b] Halim Kusumaatmaja [ID] *[c] and Kislon Voïtchovsky [ID] *[a]

Nanoparticle adhesion at liquid interfaces plays an important role in drug delivery, dust removal, the adsorption of aerosols, and controlled self-assembly. However, quantitative measurements of capillary interactions at the nanoscale are challenging, with most existing results at the micrometre to millimetre scale. Here, we combine atomic force microscopy (AFM) and computational simulations to investigate the adhesion and removal of nanoparticles from liquid interfaces as a function of the particles' geometry and wettability. Experimentally, AFM tips with controlled conical geometries are used to mimic the nano-asperities on natural nanoparticles interacting with silicone oil, a model liquid for many engineering applications including liquid-infused surfaces. Computationally, continuum modelling with the Surface Evolver software allows us to visualise the interface configuration and predict the expected force profile from energy minimisation. Quantitative agreement between the experimental measurements and the computational simulations validates the use of continuum thermodynamics concepts down to the nanoscale. We demonstrate that the adhesion of the nanoparticles is primarily controlled by surface tension, with minimum line tension contribution. The particle geometry is the main factor affecting the length of the capillary bridge before rupture. Both the particle geometry and liquid contact angle determine the shape of the adhesion force profile upon removal of the particle from the interface. We further extend our simulations to explore more complex geometries, rationalising the results from experiments with imperfect AFM tips. Our results could help towards the design of smart interfaces, for example, able to attract or repel specific particles based on their shape and chemistry.

Introduction

Particles often get trapped at liquid interfaces. This naturally occurring process is important for fields as diverse as drug delivery,[1] dust removal,[2,3] aerosol inhalation,[4,5] and controlled self-assembly.[6,7] When a particle encounters a liquid interface, a meniscus forms between the particle and the surface of the liquid. Depending on the position of the particle, the meniscus can exert a capillary force that drives the particle to a position which minimises the associated interfacial free energy. The details of this process depend on the particle size and geometry, the liquid properties, and the interactions between the liquid and the particle. Experimental methods for quantifying particle adhesion often involve detaching particles from interfaces while recording the necessary force to carry the task. Initial studies mainly have focused on micron- to millimetre-sized particles with simple geometries to ensure ease of

experimental tractability with standard optical microscopy, force measurements, and a relatively straightforward implementation of capillary theory. For example, Scheludko[8] and Huh[9] investigated the force necessary to pull millimetre-sized spheres from liquid–air interfaces. By comparing experiments and theoretical force calculations derived for spherical particles, they were able to infer the liquid interfacial tension. More recent works explored different surface functionalisation to vary the liquid contact angle and different particle geometries, including cylinders, ellipsoids, pyramids, and cubes.[10–14] There is also growing interest in exploring and manipulating the interplay between multiple particles at liquid interfaces, which can interact *via* a variety of forces, including electrostatic, depletion, and capillary-mediated forces.[15–17]

Despite these advances, there remains an open question whether capillary theory can be applied at the nanoscale, in particular on the role of line tension. For instance, it has often been argued that line tension can become important in describing wetting phenomena at the nanoscale.[18,19] In contrast, Pakarinen[20] and Cappella[21] have suggested that capillary theory that only considers Laplace pressure and surface tension generally remains valid in the nanoscale systems they tested. In any case, both schools of thought highlight the necessity of comparing theoretical predictions with experimental data and investigating more complex geometries. Studying capillary

[a] Department of Physics, Durham University, Durham, DH1 3LE, UK.
 E-mail: kislon.voitchovsky@durham.ac.uk
[b] GreenChemSolution, West Chester, OH 45069, USA
[c] Institute for Multiscale Thermofluids, School of Engineering,
 The University of Edinburgh, Edinburgh, EH9 3FB, UK.
 E-mail: halim.kusumaatmaja@ed.ac.uk
† Electronic supplementary information (ESI) available. See DOI: **https://doi.org/10.1039/d4sm01101e**

phenomena at the nanoscale presents both a challenge and an opportunity: on the one hand experiments are difficult with the need to control particle geometry and the associated forces well beyond the capabilities of traditional optical approaches. On the other hand, the enhanced surface-to-volume ratio of nanoparticles offers new opportunities for interfacial targeting and related nanotechnological applications.[22,23]

To tackle this issue, we employ an experimental setup based on atomic force microscopy (AFM), a technique that measures forces down to the piconewton range. Over the last decade, AFM has often been used for studies on capillary and interfacial forces, typically attaching a microsphere or a droplet to the AFM tip to measure adhesion.[24–29] In contrast, akin to the work of Schellenberger,[29] here we use the AFM tip itself as a model nanoparticle with a controlled conical shape. Conical nanoparticles are relevant for a wide range of medical and engineering applications and can serve as a model system for nanoscale asperities on naturally occurring particles. Examples include the cone-shaped HIV-1 capsids that penetrate nuclear pore complex;[30] conical Janus particles that serve as effective stabilisers for emulsions;[31] and pollen particles with nanoscale conical spikes that exhibit strong mucoadhesion.[32]

For the liquid interface, we use liquid-infused surfaces (LIS)[33–36] with silicone oil as the lubricant. Aside from their potential for applications in technology and industry, LIS offer a good model for nanoparticle adsorption to viscous interfaces, for example in mucus and the natural biofilms in airways or in the lubricant film of moving mechanical parts. In the context of LIS, understanding the deposition and removal of nanoparticles (e.g., dust and other contaminants) has important implications for their performance and longevity. First, particles often have irregular shapes,[37,38] emphasising the need to investigate non-spherical particles. Second, nanoparticles are directly detrimental to the performance of LIS, as in the context of self-cleaning surfaces[39] or anti-fouling surfaces,[40] or because they can seed other processes, such as nucleation in anti-icing applications.[41]

Practically, we use conical AFM tips with different conical angles, with the tip characteristics independently confirmed by electron microscopy. We also interface the silicone oil with both air and water to vary the effective particle wettability. To complement our AFM experiments, we harness computer simulations set up to mimic the experimental geometry, offering a quantitative comparison of the capillary effects. This is achieved with the software Surface Evolver,[42] a continuum simulation method specialised in interfacial modelling. The simulations make it possible to quantify and visualise the intricacies of the nanoparticles' adhesion to the liquid interfaces and are used to systematically evaluate the impact of different interfacial and line energy contributions, as well as that of the particles' geometrical features.

Materials and methods

Fabrication of liquid-infused surfaces (LIS)

The LIS used in this study is composed of a porous solid base infused with a thin film of lubricant on top. The base is formed by layered hydrophobic nanoparticles, and the lubricant is silicone oil.[33,34] The LIS substrates were fabricated as follows. First, rectangular glass slides (24 × 60 mm, Deckgläser, VMRTM, Lutterworth, UK) were sonicated in deionised water (18.2 mW, Merck-Millipore, Hertfordshire, UK) for 30 min at 30 °C, followed by sonication in 5 w/w% Decon 90 (Merck, Sigma-Aldrich, Gillingham, UK), and deionised water again. Subsequently, the slides were rinsed consecutively with acetone (Technical, Thermo Scientific™, Cambridge, UK) and isopropanol (99.5% for HPLC, Thermo Scientific™, Cambridge, UK), and then dried under nitrogen. Second, the porous structure was created on the slides using Glaco™ (SOFT 99 Corp., Japan), a commercially available spray of hydrophobised silica nanoparticles. Glaco was sprayed across the cleaned glass slides and then dried for an hour at ambient temperature. This process was repeated until five layers of spray coating were applied to the slides. In the final step, a thin layer of silicone oil was infused on the porous substrate. Three drops (approx. 0.15 mL) of silicone oil (10 cSt at 25 °C, Merk, Sigma-Aldrich, Gillingham, UK) were deposited on a slide and subsequently spin-coated for 1 min at 1000 rpm, followed by 1 min at 500 rpm. LIS fabricated through this process retains an oil layer thickness of more than 3 μm in 16 days after fabrication,[33] which is sufficient to prevent contact between the tip and the underlying porous structure during our experiments.

AFM setup and experimental strategy

Adhesion force curve measurements were conducted using two commercial AFMs: a Cypher ES (Oxford Instruments, USA) and a JPK NanoWizard 3 (Bruker, USA). Individual tips (Spark 70, Nu Nano Ltd, Bristol, UK; SNL-10, Bruker, USA) were used in each measurement. The Spark 70 tips are platinum-coated silicon tips, whereas the SNL-10 tips have silica surfaces in ambient conditions. All measurements used for quantification were conducted using Cypher ES AFM with Spark 70 tips at a controlled temperature of 30.0 ± 0.1 °C, except for the one involving imperfect geometry (see Fig. 7b), which was carried out using JPK NanoWizard 3 with an SNL-10 tip. Every Spark 70 was pre-characterised using electron microscopy, and we primarily selected tips with axisymmetric conical shapes to ensure reproducibility of the measurements across different setups. The tip cone angle near the apex varies from 10° to 38°, as measured from electron microscopy images using the ImageJ freeware.[43] Before each experiment, the tip was rinsed with isopropanol alcohol and then UV-treated for 5 minutes to gently remove organic contaminants from the manufacturing process and storage box. Each force spectroscopy measurement (see Results section for details) was repeated at least ten times, always moving at a constant velocity of 100 nm s⁻¹ to allow quasi-equilibrium of the system (see Fig. S1 of the ESI† for the velocity choice). This procedure yielded reproducible results, as the capillary bridge between the tip and the surface of the liquid was elongated and subsequently ruptured (see Fig. S2 of the ESI† for an example set of data). After the desired measurements were completed, the spring constant and sensitivity were systematically characterised on a clean glass slide using the

thermal method.[44] We obtained cantilever spring constant for Spark 70 tips used in this study in the range 0.75–2.38 N m^{-1} (resonance frequency of 44–63 kHz in air). The SNL-10 tip used has a spring constant of 0.39 $\pm$ 0.05 N m^{-1} (resonance frequency 64.18 kHz in air).

Experimental determination of the liquid–solid contact angles

Due to the nano- to micro-scale size of the AFM tips and cantilevers, direct contact angle measurements are not feasible. Instead, we measured the contact angle by depositing a droplet of silicone oil on surfaces composed of same material as the tip. A platinum film (99.99%, Sigma-Aldrich, Gillingham, UK) was used to replicate the tip surface of platinum coated tip Spark 70, while a silicon wafer (n-type, Inesto, Hampshire, UK) represented the silica surfaces of the silicon nitride SNL-10 tip. In ambient air, the silicone oil exhibits nearly complete wetting (contact angle $\theta \sim 0°$) on both the platinum film and silicon wafer (see Fig. S3 of the ESI† for further details). For convenience, we typically assumed $\theta = 5°$ in the simulation model to directly compare with the experimental measurement in air (Fig. 3). This is justified because the force profile does not exhibit a significant difference when we carry out simulations from $\theta = 3°$ to $\theta = 10°$ (see Results). For measurements in water, the contact angle was measured by injecting a drop of oil onto the surfaces from below, in an upside-down configuration. We found $\theta = 106.5 \pm 3.8°$ (see Fig. S4 of the ESI†).

Surface Evolver

We used the Surface Evolver[42] to determine the energy and configuration of a system comprising a solid truncated cone as a function of the particle position from the liquid interface (Fig. 1). This mimics pulling the particle off the interface in the quasi-static limit. In Surface Evolver, each interface is triangulated. Subsequently, suitable interfacial and line tension energy contributions can be assigned to the facets and edges of the triangles.

In our simulations, the cone angle α is adjusted to mimic the AFM tips (cone angle $\alpha = 12°-38°$). The liquid contact angle θ on the particle surface was set in the range of $30°-115°$ to investigate the effect of liquid wettability on the particle (see diagram in Fig. 1a). The contact angle is related to the interfacial tensions via the well-known Young's equation, $\gamma_{SL} = \gamma_{SG} - \gamma_{LG}\cos\theta$, with γ_{SL}, γ_{SG} and γ_{LG} referring to the interfacial tensions (or energies) for the solid–liquid, solid–gas (or other surrounding fluid) and liquid–gas (or other surrounding fluid) interfaces, respectively. Since the capillary length of silicone oil is $\lambda = 1.48$ mm in air and $\lambda = 7.14$ mm in water ($\lambda = \sqrt{\gamma/\Delta\rho g}$, with $\gamma_{oil-air} = 20$ mN m^{-1}, $\gamma_{oil-water} = 35$ mN m^{-1}, $\rho_{oil} = 930$ kg m^{-3}, $\rho_{water} = 1000$ kg m^{-3}, and $g = 9.8$ m s^{-2}), gravity can be neglected in the nanoscale measurement and hence ignored in the simulations. In several cases, we also included line tension energy as an extra free energy term associated with the three-phase contact line. We varied the line tension energy from $|\tau| = 1 \times 10^{-12}$ N to 1×10^{-6} N, encompassing a wide range of possible magnitudes reported in the literature.[19,45–47]
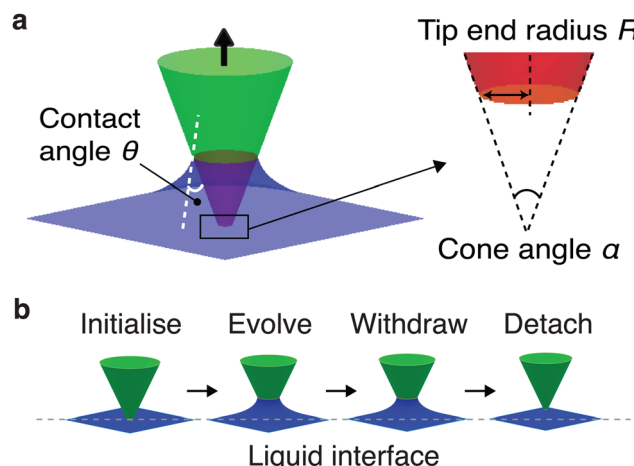

Fig. 1 Surface Evolver simulation set up. (a) The desired particle geometry, here a truncated cone, is highlighted in green above the liquid, with the immersed part of the particle shown in red inside the liquid, and the liquid interface visible in blue. Particles with a cone angle α in the range of $12-38°$ and a contact angle θ of $3-115°$ with the liquid were investigated. (b) The system was initialised with the tip apex immersed into the liquid, followed by relaxation of the interface and then progressive withdrawal of the tip away from the surface.

The system was initiated with the tip already indented in the liquid. A Surface Evolver script which provides a routine of energy minimisation iteration (using gradient descent) and mesh refinement was written to achieve an equilibrium state by evolving the liquid to form a meniscus around the tip (Fig. 1b). The tip was then withdrawn in a fine, stepwise manner, with the energy of the system minimised at each tip position. For each step, the tip moves incrementally upwards along the z-direction by 1% of its own height per step. This allows for a gradual evolution of the system, ensuring that the mean curvature evolution of the liquid interface is accurately captured throughout the retraction process with sufficient datapoints. The liquid interface evolves and relaxes in a gradient descent manner to minimise the total energy of the system, considering both surface tension and geometric constraints. The equilibrium configuration from the previous step serves as the initial condition for the energy minimisation, effectively mimicking the retraction process of the AFM experiment (Fig. 1b). An example Surface Evolver script is provided as ESI† S4.

Results and discussion

AFM force spectroscopy measurement

AFM force spectroscopy measurements enable precise quantification of the adhesion force experienced by the tip as it enters and is subsequently removed from the interface. During a typical measurement, the AFM tip initially approaches the silicone oil surface from the air or pure water. Upon contact, a capillary meniscus forms around the tip, exerting a vertical capillary force. The tip is then withdrawn, and the meniscus elongates until it ruptures (Fig. 2a). The capillary force deflects
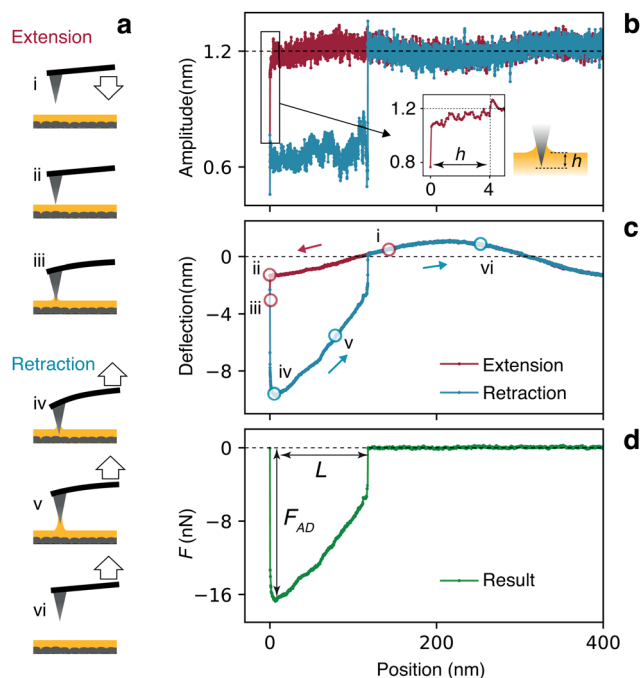
Fig. 2 Example of a typical AFM force spectroscopy measurement. (a) Schematic representation of the measurement process: the cantilever and tip approach the surface of the liquid at a constant velocity (i) until contact is made (ii). This leads to the formation of a meniscus and a net force acting on tip, inducing a static deflection on the cantilever (iii). The capillary force draws the tip deeper into the liquid as the cantilever is being retracted (iv). Upon retraction, the capillary meniscus is extended into a bridge (v), which eventually ruptures (vi), allowing the cantilever deflection to return to zero. (b) By superimposing a small oscillation on the cantilever's static deflection, the point of contact between the tip and the liquid can be accurately and dynamically detected, allowing for an immediate retraction trigger. An example of a measurement is shown for the amplitude acting as a trigger and the static deflection acquired simultaneously (c), indicating the different stages of the measurement. From the static deflection, the capillary force can be readily obtained by multiplication with the spring constant of the cantilever (d). L represents the maximum capillary bridge length, and F_{AD} represents the maximum adhesion force. In this example, the trigger point is reached once the amplitude has decreased to 60% of its value in air, leading to an indentation depth into the liquid of $h \sim 4$ nm.

the cantilever, allowing quantification of the force's magnitude and direction. Additionally, the precise position of the tip relative to the point of contact can be determined from the combined measurement of the cantilever base position and its deflection.[14,25,48] Here, since we aim for nanometre-level precision in our measurements, careful control over the indentation depth h at which the tip dips into the interface is needed (Fig. 2b, inset). This is challenging due to the fluid nature of the interface and the ability of the liquid to form a moving capillary bridge with the tip apex. To overcome this issue, we employ dynamic sensing strategy whereby the tip is externally oscillated close to the resonance frequency of the cantilever. As the tip contacts the liquid, the formation of a capillary bridge instantaneously quenches the free oscillating amplitude due to the significant difference in viscosity between the fluid media: the dynamic viscosity of air and water are respectively $\mu_{air} = 0.018$ cP and $\mu_{water} = 0.89$ cP at 25 °C, at least an order of magnitude lower

than that of the LIS oil ($\mu_{oil} = 9.3$ cP at 25 °C). By setting a trigger on the cantilever amplitude, it is possible to control h with nanometre-level precision (Fig. 2b). The magnitude of the capillary force is then measured from the static (average) deflection of the cantilever, with the free oscillation amplitude kept small (< 1.2 nm, Fig. 2b) compared to static deflection (typically > 8 nm, Fig. 2c) to minimise possible crosstalk. Depending on the coating and geometry of the cantilever, the deflection baseline may show small sinusoidal oscillations (Fig. 2c) due to optical interferences from the laser measuring the cantilever deflection. These can be removed by subtracting the retraction part of the curve from the extension part. If necessary, the deflection is further filtered to remove the oscillations associated with the dynamic sensing (Fig. S5 of the ESI† for details). In the resulting force curve (Fig. 2d), the maximum force encountered by the tip is defined as the particle's maximum adhesion force F_{AD}, representing the force required to overcome the capillary adhesion and detach the particle from the interface. The maximum capillary bridge length L is the capillary bridge length before rupture, as indicated by tip displacement from the interface (Fig. 2d). It is worth noting that the vertical feature observed at the very beginning of the force curve in Fig. 2c and d arises the finite response time of the trigger and the turnaround between the approach and retraction phases. This transition happens too rapidly for precise control of the tip indentation and is not captured by our quasi-static computational model. This onset of the retraction has therefore been excluded from Fig. 3 and subsequent figures.

Comparing experimental results with computer simulations

To complement the AFM measurements, computer simulations were conducted with Surface Evolver. The goal is to enable detailed insights into the nanoparticle detachment from the liquid interface. An exemplar result, presented in Fig. 3, shows the comparison for an axisymmetric cone-shaped tip (Spark 70) with a truncated radius of $R = 28 \pm 4$ nm and cone angle of $\alpha = 30 \pm 8°$, determined through electron microscopy. The contact angle between the liquid and the tip is taken as $\theta = 5°$ to represent the highly wetting behaviour of silicone oil on a platinum film (see Methods). These experimental parameters are then imposed into the Surface Evolver simulations (see Methods). The orange-shaded area in the simulation results corresponds to the uncertainty in the experimental cone angle measurements (Fig. 3a).

The simulations are conducted in the quasi-static limit. This is justified by the fact that experimentally, the tip is moved with a constant velocity of 100 nm s^{-1} on approach and retraction. This slow velocity aims to strike a compromise between keeping the system close to equilibrium while limiting thermal drift over the relatively long travel distance (> 1 µm). Viscous forces are negligible compared to interfacial forces, as indicated by the small capillary numbers: $Ca = 4.65 \times 10^{-8}$ (oil–air) and $Ca = 2.66 \times 10^{-8}$ (oil–water).

As immediately obvious from Fig. 3, a close quantitative agreement between experiments and simulations can be
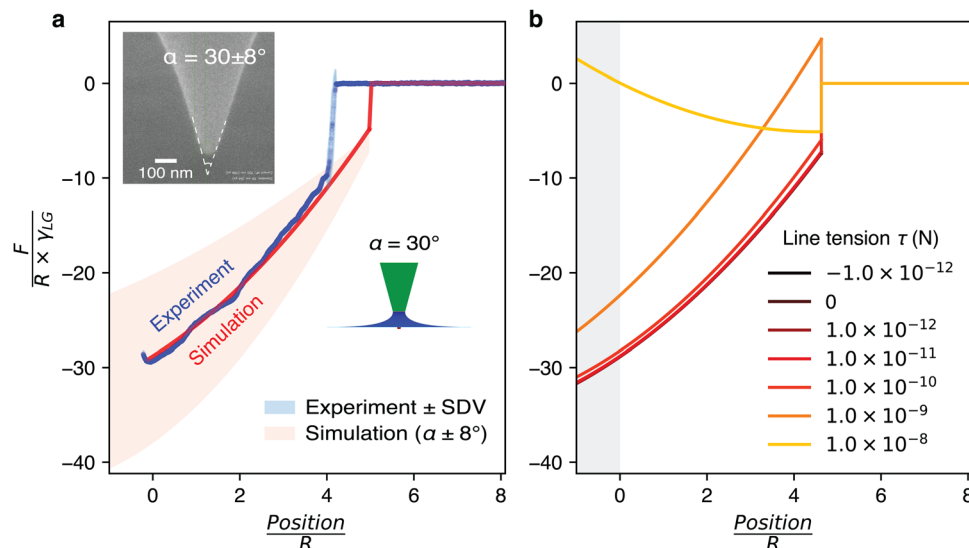
Fig. 3 Quantitative comparison of simulations and experiments conducted with the same tip geometry. The simulations were first conducted without taking into consideration line tension (a). An electron microscopy image of the tip is shown in inset, indicating a cone angle of $\alpha = 30 \pm 8°$ and an end radius of $R = 28 \pm 4$ nm. The liquid–air interface is taken as the reference point, indicating where the tip-liquid separation is zero. The x-axis (tip position relative to the liquid interface) is normalised by R, and the y-axis (measured force) by the product of $R \times \gamma_{LG}$, rendering both axes unitless. Experimental measurements were repeated twenty times and subsequently averaged to minimise random fluctuations. The orange-shadowed area around the simulated curve indicates the maximum error based on the experimental cone angle uncertainty ($\pm 8°$). The contact angle between the liquid and the tip is $\theta = 5°$ in the simulation. (b) Further simulations are performed including the line tension τ, varying from $\tau = -1 \times 10^{-6}$ to 1×10^{-6} N. The simulated force curves with -1×10^{-12} N $\leq \tau \leq 1 \times 10^{-10}$ N are indistinguishable and correctly reproduce the experimental results shown in (a). When 1×10^{-9} N $\leq \tau \leq 1 \times 10^{-8}$ N, the line tension significantly influences the force profile which no longer reproduces the experimental results. For $\tau \leq -1 \times 10^{-11}$ N and $\tau \geq 1 \times 10^{-7}$ N (not shown), the simulated system becomes too unstable to reach a static state. Note that Position/$R = 0$ corresponds the point where the tip apex meets the liquid interface when at rest. The shaded grey region represents the range where the tip end is immersed. Experimentally, the immersion depth is negligible compared to the length of the capillary bridge. Comparison with the simulations should therefore be taken outside the grey-shaded area.

obtained when assuming the same parameters. The experimental data is not as smooth as the simulated curve, but this disparity can be explained by the nanoscale surface imperfections of the AFM tip. While the effect is minimised by our use of relatively low velocities (see Fig. S1 of the ESI† for more details), local imperfections are still omnipresent on any polycrystalline surface such as the AFM tip, even if too small to be seen in the electron microscopy image.

In addition, the tip apex differs from the ideal sharp truncation used in the simulations (Fig. 2), with the experimental tip often assumed to be pseudo-spherical.[49,50] To some extent, this can be addressed by adjusting the simulated geometry. Variations in the precise shape of the apex leads to differences between experimental and simulated rupture of the capillary bridge (see Fig. S6 of the ESI†). The emphasis is therefore placed on the retraction force profile rather than the bridge rupture where nanoscale geometrical details dominate.

An important point of the simulated curve shown in Fig. 3a is that no line tension has been considered. The concept of line tension, first introduced by Gibbs as an additional free energy term at the three phase contact line,[51] can play an important role in surface and wetting phenomena.[18,19] However, the magnitude and sign of line tension remain controversial to date, with the magnitude of theoretical and simulation values ranging from $|\tau_{\mathrm{sim}}| = 1 \times 10^{-12}$ to 1×10^{-10} N and experimental

values from $|\tau_{\mathrm{exp}}| = 1 \times 10^{-12}$ to 1×10^{-6} N.[19,45–47] Here, given the nanometre scale of the system, line tension could in principle play a role. We therefore conducted simulations for a range of line tension values in addition to the usual interfacial energy contributions. We explore line tensions in the range of $|\tau| = 1 \times 10^{-12}$ N to $|\tau| = 1 \times 10^{-6}$ N (Fig. 3b). The results show that for values in the range of $-1 \times 10^{-12} \leq \tau \leq 1 \times 10^{-10}$ N, the contribution of the line tension term is negligible in the simulations. In fact, this provides the bounds for the magnitude of a possible line tension contribution in our system. Outside these bounds, if $1 \times 10^{-9} \leq \tau \leq 1 \times 10^{-8}$ N, the simulation predictions are no longer able to reproduce our experimental observations. This suggests that no significant contribution from the line tension to the adhesion force profile is experimentally present in our system. Furthermore, when $\tau \leq -1 \times 10^{-11}$ N or $\tau \geq 1 \times 10^{-7}$ N, the simulations exhibit high fluctuations, making it difficult to reach a static state and reliable predictions. The associated results are hence not presented in Fig. 3b.

While negligible in the present system, line tension can play a significant role for nanoparticles at interfaces depending on its size.[19,45–47] A simple criterion can be obtained from the ratio of τ/γ for a given interface, with line tension becoming significant for particles exhibiting a radius $R < \tau/\gamma$.[45] Here, using the upper estimate derived for τ and the measured air–oil and water–oil interfacial tensions yields a maximum value of $R \sim$

5 nm. This is below the size of our tip particles end radii which apex are in the range of $R = 25$–31 nm. Using sharper tips with a truncated radius $\lesssim 5$ nm would require taking the line tension into consideration.

Impact of tip-particle cone geometry

Having established the suitability of our dual AFM-simulation method to investigate the detachment of nanoparticles from liquid interfaces, we now focus on the particle's shape. In practice, the number of parameters that can be controlled experimentally is limited, with this section investigating the impact of the cone angle α. We therefore selected two AFM tips with significantly different cone angles. The tips and cantilever are the same by design, but we selected on purpose outliers from the average commercial production (see Methods), choosing those with cone angles of $\alpha = 30 \pm 8°$ (same data as in Fig. 3) and $\alpha = 14 \pm 2°$. For the simulations, we varied the tip cone angle from $\alpha = 12°$ to $\alpha = 38°$.

The experimental results are shown in Fig. 4a, demonstrating that the geometry of nanoparticles significantly influences their adhesion profile to the surface of the liquid. The sharper cone (smaller α) exhibits lower adhesion than the wider cone and the maximum capillary bridge length increases with α. Moreover, for the sharper cone, the adhesion force profile remains relatively constant during retraction until rupture of the capillary bridge. For the wider code, the capillary force magnitude gradually decreases (becoming less negative in the figure) upon retraction until the bridge is ruptured and the tip is fully withdrawn from the liquid.

The simulations corroborate the experimental observations as α is systematically varied (Fig. 4b). We note that the non-monotonic evolution of the normalised maximum capillary bridge length L/R with α is due to the normalisation process enabling direct comparison of the simulations with the experiments; non normalised curves show a monotonic dependence as can be expected from the theory (see Fig. S7 of the ESI†). Both the normalised force profile $F/(R \times \gamma_{LG})$ and the slope of the force increase with α. This is to be expected with wider cones presenting a larger, but height-dependent contact area with the liquid compared to sharper cones. Conversely, when the cone shape approaches that of a cylinder, the meniscus area hardly changes upon retraction, and the normalised force profile $F/(R \times \gamma_{LG})$ varies little until the bridge ruptures. Interestingly, the experimental results indicate a cylinder-like behaviour already at $\alpha \sim 14°$. This can be explained by the imperfect shape of the tip (Fig. 4a inset), with the slight reversal of the cone shape near the tip apex. The effect is likely subtle, and local variations in the tip-liquid contact angle could also be responsible for this effect, as explored in the next section.

Impact of the tip-liquid contact angle

Aside from the shape of the particle tip, the contact angle θ formed by the liquid (here the oil) with the surface of the particle offers another crucial factor affecting adhesion at the
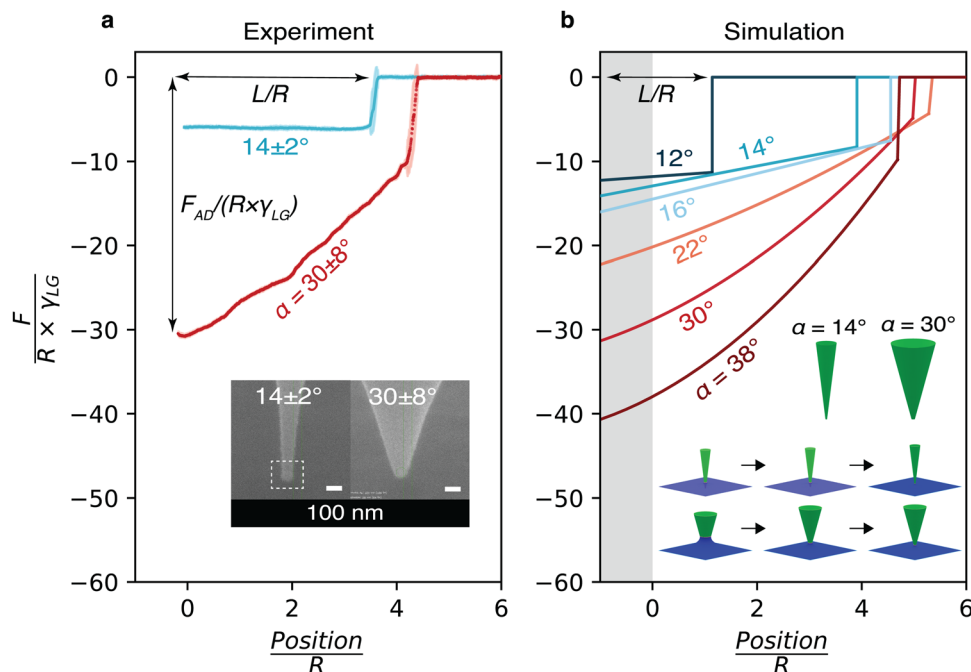

Fig. 4 Effect of the cone angle on the adhesion force of the tip at the air–LIS interface. The experiments in (a) are conducted with platinum-coated tips exhibiting a cone angle of $\alpha = 30 \pm 8°$ and $\alpha = 14 \pm 2°$ (see electron microscopy images, with a slight reversal geometry at the apex highlighted by a dash-line square). The simulations (b) are conducted with $\theta = 5°$ and varying cone angle α in the range of 12–38°. The contact angle with the oil is assumed to be $\theta = 5°$, consistent with measurements on flat surfaces and results in contact angle discussion (see Methods and results). The inset shows simulation frames for cone angles of $\alpha = 14°$ and $\alpha = 30°$ during withdrawal from the liquid interface. All quantities have been normalised as in Fig. 3 to make them unitless. The grey-shaded area indicates the part of the curve with the tip apex below the liquid's surface. L/R represents the normalised maximum capillary bridge length, and $F_{AD}/(R \times \gamma_{LG})$ represents the normalised maximum adhesion force.

interface. θ quantifies the liquid ability to wet the tip surface and hence influences the capillary force. To quantitatively explore this parameter, we used the same dual AFM-simulation approach: experimentally, systematically varying θ is challenging, but two values could be explored with the same tip by comparing curves obtained at the air–oil ($\theta \sim 0°$) and water–oil ($\theta \sim 106°$) interfaces (Fig. 5). From the electron microscopy image, the tip used for this set of experiments exhibits an average cone angle of $\alpha = 26 \pm 4°$, with simulations conducted imposing $\alpha = 26°$. It should be noted, however, that this conical tip is not perfectly axisymmetric (see Fig. S8 of the ESI†) with small variations in α visible, depending on the side of the tip observed. We believe these variations to be responsible for the imperfect match between the experimental results and the simulations. In the simulations we systematically varied the contact angle from $\theta = 3°$ to $\theta = 115°$, which captured well the range of possible experimental contact angles once measurement uncertainties are taken into account.

For the sake of clarity, we hereafter refer to oil as the liquid, and the air or water (tip approach medium) as the fluid. The measured force is normalised by liquid–fluid interfacial tension γ_{LF} and the tip apex radius R, where $\gamma_{LF} = 20$ mN m^{-1} for an oil–air interface and $\gamma_{LF} = 35$ mN m^{-1} for an oil–water interface. The results indicate good agreement between simulation predictions and experimental observations, with a general trend of the magnitude of $F/(R \times \gamma_{LF})$ decreasing (becoming less negative) with increasing θ – the intuitive fact that lower wettability benefits removal from the interface (Fig. 5). Comparing the force curves highlights the complexities as we vary the contact

angle, with a reversal of the shape of the force profile depending on the specific value of θ.

The systematic simulation study (Fig. 5b) reveals three main regimes when withdrawing the particle from the interface. For $\theta \leq 53°$, the strong affinity of the liquid for the tip creates a large capillary meniscus, resulting in an instantaneous adhesion $F/(R \times \gamma_{LF})$ when the tip 'touches' the surface of the liquid. Withdrawal of the tip away from the surface induces a monotonic decrease in the magnitude of the capillary force with a steeper gradient before detachment of the bridge. This behaviour is dominated by the sliding of the three-phase contact line along the conical particle before it reaches the tip apex, similar to the situation presented in Fig. 4 (see Fig. S9 of the ESI† for details on various interfacial energy contributions).

For $53° < \theta < 97°$, the force profile becomes non-monotonic. The force profile can be divided into two stages. Firstly, before the contact line reaches the apex of the tip, the capillary force magnitude decreases (becoming less negative), driven by the combined contributions of the three interfaces as the contact line slides along the conical particle, along with a slight increase of the liquid–fluid interfacial area (see ESI† Fig. S9). Secondly, once the contact line is pinned at the truncated cone apex, the capillary force behaviour shifts to being dominated solely by the liquid–fluid interface (see ESI† Fig. S9), leading to an increase in the capillary force (more negative value) until complete detachment.

For $\theta \geq 97°$, the force curve is dominated by the liquid–fluid interface after the contact line reaches the tip apex (see Fig. S9 of
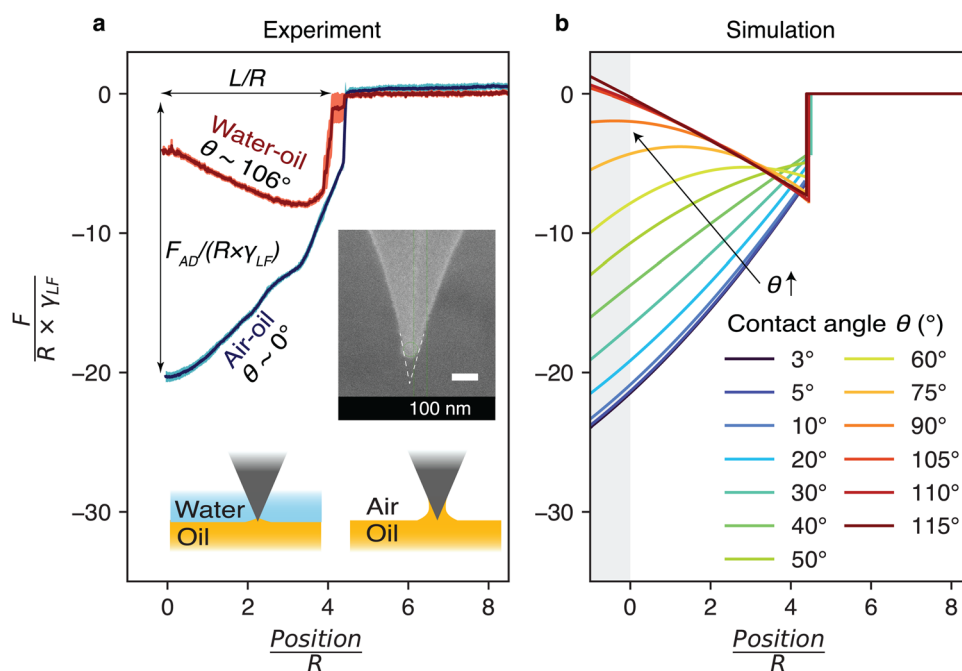

Fig. 5 Impact of the contact angle θ between the liquid and the tip on the measured adhesion force profile. (a) Experimentally, two θ values are explored by varying the approach fluid in contact with the LIS:air and water (cartoons in inset). Position and force axes are normalised to be unitless as in the previous figures. The simulation results (b) are obtained by systematically varying θ with a conical tip of angle $\alpha = 26°$ to compare with the experimental result. The shaded grey area represents the region where the tip apex is below the surface of the oil. L/R represents the normalised maximum capillary bridge length, and $F_{AD}/(R \times \gamma_{LF})$ represents the normalised maximum adhesion force.

the ESI†). As a result, the capillary force behaves monotonically again. The force magnitude increases (becoming more negative in Fig. 5b) until the rupture of the bridge. Interestingly, comparing cone angle variation in Fig. 4b and contact angle variation in Fig. 5b, we found that the maximum capillary bridge length before rupture is primarily governed by the cone angle α, while the impact of the contact angle θ is negligible. This indicates that the amplitude of the vertical movement required to detach the particle from the interface is almost independent of the wetting properties of the liquid.

Towards more realistic systems

The results presented in the previous sections generally achieve good quantitative agreement between experiments and simulation. This is possible thanks to the ideal axisymmetric AFM tips used, although imperfections in the tip geometry and composition already show in the experimental curves. This is exemplified in Fig. 5 where electron microscopy highlights defects in the desired axisymmetric geometry (see Fig. S8 of the ESI† for details). Generally, real-life nanoparticle–liquid interfaces are non-ideal. Most solids exhibit chemical heterogeneities or geometric imperfections at the nanoscale, ranging from sharp edges to multiple facets with different chemical properties. Each of these factors can influence the force profile, sometimes with distinctive features that differentiate them from the simple cone model. Systematically examining the impact of nanoscale geometrical and chemical variations is experimentally challenging. However, our simulations offer the ideal tool for such a study, having been validated with experiments on simple regular geometries.

Here, motivated by scenarios that can be anticipated in our AFM experiments, we explore two common experimental scenarios. First, we investigate the impact of a systematic shape alteration whereby a cone is progressively turned into a square pyramid (4 facets and edges) – most AFM tips are pyramidal. Mathematically, we do this by employing the following shape relation:[52]

$$x^2 + y^2 - \frac{s^2 c^2 x^2 y^2}{z^2} = \frac{z^2}{c^2}$$
$$\left(0 \le z \le c, \; -\frac{z}{c} \le x \le \frac{z}{c}, \; -\frac{z}{c} \le y \le \frac{z}{c} \right) \quad (1)$$

where $c = 3$, x, y, and z are the three coordinates defining the particle surfaces, and s is the so-called shape factor. Depending on the value of s, the surface of the particle can be a cone ($s = 0$), a square pyramid ($s = 1$), or something in-between termed a squircular cone (or sqone) for $0 < s < 1$.

Simulated force-distance curves are obtained systematically varying s from 0 to 1 (Fig. 6a). The results show an increase in the maximum adhesion force as the cone particle transitions towards a pyramid, also leading to a steeper slope. There are two ways to normalise the tip position, either by using the width of the tip apex R or by using the equivalent radius (effective radius) R' of a circle that has the same perimeter as the sqone tip apex. Here, by choosing the latter we observed a decrease in the normalised maximum capillary bridge length L/R' before rupture with increasing shape factor s. However, as discussed in ESI† S10, if we choose to normalise with R, L/R becomes invariant with s. This underscores once again that the capillary bridge rupture length depends sensitively on the details of the tip apex. Comparatively, varying the cone angle appears to have a much larger impact on the magnitude of the adhesion force (as discussed in Fig. 4b).

Second, in AFM experiments, the tip (nanoparticle) often approaches the liquid interface not perpendicularly, but at a tilt
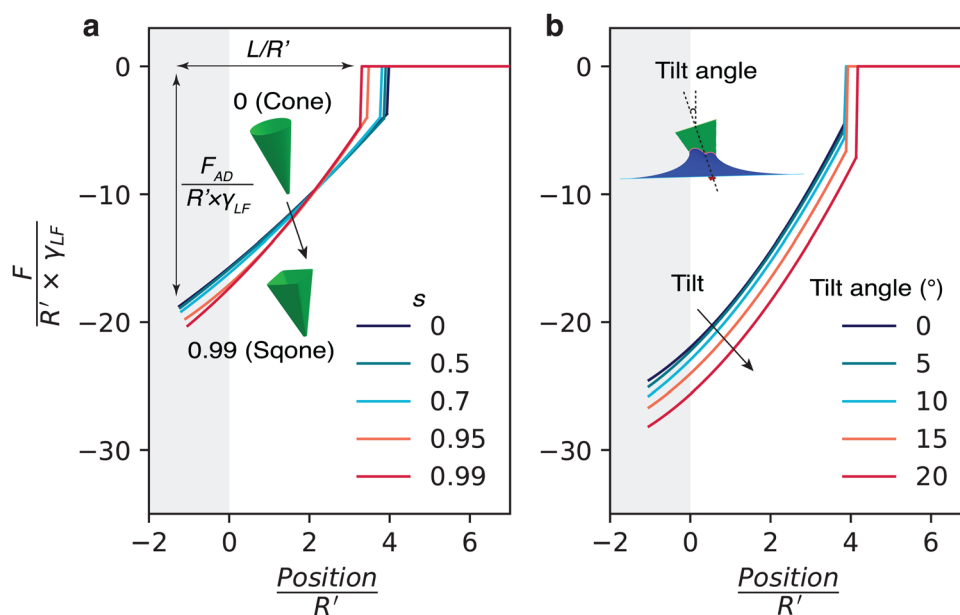

Fig. 6 Simulation of the adhesion profile of more realistic nanoparticle–interface situations. (a) Variation of the shape factor s tuning a cone to a pyramid. (b) Tilting of the interface with respect to the axis of the particle. Both position and force axes are normalised to be unitless. L/R' represents the normalised maximum capillary bridge length, and $F_{AD}/(R' \times \gamma_{LF})$ represents the normalised maximum adhesion force.
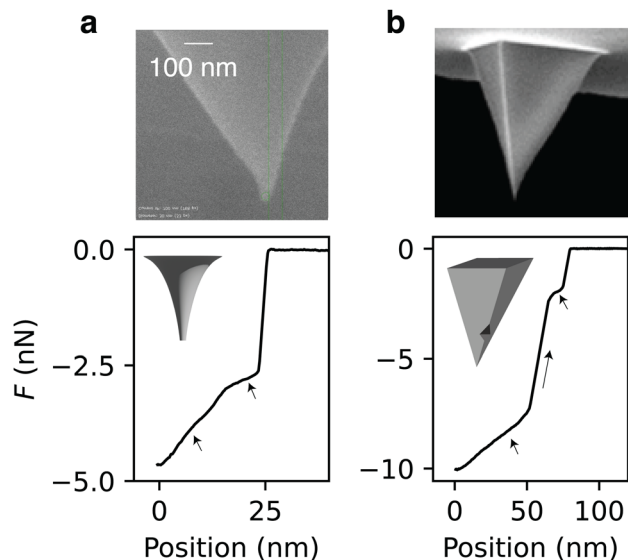
Fig. 7 Examples of force curve features for imperfect particles in the experiment. (a) Retraction of an imperfect Spark 70 tip from an air–oil interface exhibits local decreases in the slope of the force profile (see arrows), likely due to a decrease in the effective tip cone angle as it emerges from the oil (electron microscopy image of the tip). A cartoon illustrates the possible cone angle variation on the tip (inset). (b) Retraction of a pyramidal SNL-10 tip shows a stepwise motion (see arrows), likely due to pinning by local geometrical imperfectness or pyramid edges. A cartoon depicts the design of the pyramidal tip with a geometrical imperfection. The electron microscopy is a general SNL-10 image from Bruker,[53] reproduced with permission.

angle. In this case, as shown in Fig. 6b, the shape of the force profile remains largely unchanged, but the magnitude of the force increases with the increase of the tilt angle due to the larger overall interface. The maximum capillary bridge length slightly increases with the tilt angle.

General discussion for imperfect particles

Nanoparticle adhesion at liquid interfaces is a complex process where small changes can significantly alter the force profile. Here we build on the variations in geometry and wettability systematically investigated in the previous section to help interpret experimental measurements on non-ideal particles: an irregular conical Spark 70 tip and a pyramidal SNL-10 tip (see Methods). Although the Spark 70 tip is perfectly conical by design, its manufacture can occasionally lead to irregular tip shapes, as visible in Fig. 7a: the tip is sharp at the apex, but it becomes wider and loses its axisymmetry away from the apex. In a retraction process from the interface, the cone angle of the tip decreases as the contact line moves downwards to the apex (Fig. 7a). This results in a decreased force slope before the rupture of the bridge (Fig. 7a, see arrows), which aligns with the force profile's dependence on cone angle variation as shown in Fig. 4b. Another possible explanation is some chemical heterogeneity of the tip: the contact angle may be higher at the apex and lower at the bottom due to an imperfect platinum coating, causing the force slope to decrease.

As another example, a pyramidal tip SNL-10 exhibits a stepwise pattern in its force profile during retraction (Fig. 7b). The steps (Fig. 7b, see arrows) are characterised by sharp changes in the slope, which then returns to its original value. This phenomenon is likely due to local geometric imperfections on the tip surface that introduce contact line pinning or tilting between the particle and the interface, hence introducing shifting in the force axis (as in the example in Fig. 6b).

Beyond these to simple examples, real-world systems such as dust particles and engineered functional nanoparticles are likely to have even greater variations in size, geometry, and heterogeneity, something that can significantly impact their adhesion profile, as illustrated in this study. A systematic investigation of these effects would require precise control over the tip's surface features down to the nanoscale. This can in principle be achieved through set geometric modifications[54] or controlled chemical alterations of the surface.[55]

Conclusions

In this work, we have explored nanoparticle adhesion at liquid interfaces using experimental and computational simulation approaches. Using dynamic sensing with AFM we measured the adhesion force profile of nano-cones at liquid interfaces. Continuum simulations of the experiments quantitatively match the experimental results for simple nanoparticles geometries.

We found that the adhesion force increases with the angle of the nano-cone, and with a decrease in contact angle between the liquid and the material composing the tip. The maximum length of the capillary bridge increases significantly with an increase in cone angle, but remains weakly dependent of the liquid wettability on the particle. This indicates that both particle geometry and interfacial properties contribute to the adhesion force of nanoparticles at a liquid interface, with geometry playing a dominant role in the capillary rupture during detachment.

This investigation fills a gap in understanding of capillary adhesion phenomena for nanoparticles at liquid interfaces, demonstrating that classical thermodynamics still holds quantitatively at the nanoscale, with no significant contribution from the line tension. This enabled us to establish a bound of -1×10^{-12} N $< \tau < 1 \times 10^{-10}$ N for the line tension of our system, in line with both experimental and theoretical values in the literature.[19,45–47] A more detailed quantification of line tension would require complete control of the nanoscale geometry and chemistry in combination with molecular-level simulation, such as molecular dynamics. Here, nanoscale effects reveal themselves primarily through local tip imperfections inducing fluctuations in the experimentally measured force profile, but these effects cannot be controlled within error. In some cases, the effects can also be simply explained by geometrical effects or 'effective' wetting properties.

We believe this work could provide guiding principles for design of smart interfaces. For example, these interfaces could be capable of attracting or repelling specific particles based on

their shape and chemistry. The present results demonstrate that simulations could help derive effective surface properties of an unknown particle by matching experimental measurements with a range of possible simulation predictions. This foundation could be further expanded by exploring other liquid interface combinations and investigating more complex particles, such as those with controlled irregular surface geometries or varied wettability (contact angles) across different facets. Beyond single-particle behaviour, our simulation model could also be extended to investigate particle–particle interaction at the liquid interfaces.[11] Additionally, the experimental approach described here can also be easily adapted to explore dynamic effects, for example due to high viscosities of the fluid interfaces. However, addressing such dynamic phenomena computationally would require different approaches such as computational fluid dynamics (CFD)[56] or the Lattice Boltzmann method.[57,58]

Author contributions

The study was designed by KV and HK. KS performed all the measurements and simulations, and analysed the data with the help of KV (experiments) and HK (simulations). YG commented on the results and advised the study. KS, KV and HK wrote the manuscript with inputs from YG.

Data availability

Data for this article, including AFM and simulations measurements as presented in Fig. 2–7 are available at Durham University's Research Data Repository (**https://doi.org/10.15128/r2rx913p95d**) at **https://collections.durham.ac.uk/files/r2rx913p95d**. An example of the software script used for the simulations is provided as ESI.†

Conflicts of interest

The authors declare no conflict of interest.

Acknowledgements

References

1 C. de Souza Carvalho, N. Daum and C.-M. Lehr, *Adv. Drug Delivery Rev.*, 2014, **75**, 129–140.

2 T. Heckenthaler, S. Sadhujan, Y. Morgenstern, P. Natarajan, M. Bashouti and Y. Kaufman, *Langmuir*, 2019, **35**, 15526–15534.

3 C. Gómez Suárez, J. Noordmans, H. C. van der Mei and H. J. Busscher, *Langmuir*, 1999, **15**, 5123–5127.

4 S. Bakand, A. Hayes and F. Dechsakulthorn, *Inhalation Toxicol.*, 2012, **24**, 125–135.

5 Y. Fujitani, Y. Sugaya, M. Hashiguchi, A. Furuyama, S. Hirano and A. Takami, *J. Aerosol Sci.*, 2015, **81**, 90–99.

6 D. S. Frost, E. M. Nofen and L. L. Dai, *Adv. Colloid Interface Sci.*, 2014, **206**, 92–105.

7 Y. Fu, S. Zhao, W. Chen, Q. Zhang and Y. Chai, *Nano Today*, 2024, **54**, 102073.

8 A. D. Scheludko and D. Nikolov, *Colloid Polym. Sci.*, 1975, **253**, 396–403.

9 C. Huh and S. G. Mason, *Can. J. Chem.*, 1976, **54**, 969–978.

10 H.-J. Butt and M. Kappl, *Adv. Colloid Interface Sci.*, 2009, **146**, 48–60.

11 S. Dasgupta, M. Katava, M. Faraj, T. Auth and G. Gompper, *Langmuir*, 2014, **30**, 11873–11882.

12 P. M. McGuiggan and J. S. Wallace, *J. Adhes.*, 2006, **82**, 997–1011.

13 G. Soligno, M. Dijkstra and R. van Roij, *Phys. Rev. Lett.*, 2016, **116**, 258001.

14 P. Sudersan, M. Müller, M. Hormozi, S. Li, H.-J. Butt and M. Kappl, *Langmuir*, 2023, **39**, 10367–10374.

15 H. Cooray, P. Cicuta and D. Vella, *J. Phys.: Condens. Matter*, 2012, **24**, 284104.

16 A. Dani, M. Yeganeh and C. Maldarelli, *J. Colloid Interface Sci.*, 2022, **628**, 931–945.

17 E. Guzmán, F. Ortega and R. G. Rubio, *Langmuir*, 2022, **38**, 13313–13321.

18 M. Kanduč, L. Eixeres, S. Liese and R. R. Netz, *Phys. Rev. E*, 2018, **98**, 032804.

19 T. Pompe and S. Herminghaus, *Phys. Rev. Lett.*, 2000, **85**, 1930–1933.

20 O. H. Pakarinen, A. S. Foster, M. Paajanen, T. Kalinainen, J. Katainen, I. Makkonen, J. Lahtinen and R. M. Nieminen, *Modell. Simul. Mater. Sci. Eng.*, 2005, **13**, 1175–1186.

21 B. Cappella, *Micron*, 2017, **93**, 20–28.

22 X. Li, C. Chen, Q. Niu, N.-W. Li, L. Yu and B. Wang, *Rare Met.*, 2022, **41**, 3591–3611.

23 S. Shi and T. P. Russell, *Adv. Mater.*, 2018, **30**, 1800714.

24 J. Ally, E. Vittorias, A. Amirfazli, M. Kappl, E. Bonaccurso, C. E. McNamee and H.-J. Butt, *Langmuir*, 2010, **26**, 11797–11803.

25 S. E. Anachkov, I. Lesov, M. Zanini, P. A. Kralchevsky, N. D. Denkov and L. Isa, *Soft Matter*, 2016, **12**, 7632–7643.

26 W. R. Bowen, N. Hilal, R. W. Lovitt and C. J. Wright, *Colloids Surf., A*, 1999, **157**, 117–125.

27 D. Daniel, C. L. Lay, A. Sng, C. J. Jun Lee, D. C. Jin Neo, X. Y. Ling and N. Tomczak, *Proc. Natl. Acad. Sci. U. S. A.*, 2019, **116**, 25008–25012.

28 T. Jiang and Y. Zhu, *Nanoscale*, 2015, **7**, 10760–10766.

29 F. Schellenberger, P. Papadopoulos, M. Kappl, S. A. L. Weber, D. Vollmer and H.-J. Butt, *Phys. Rev. Lett.*, 2018, **121**, 048002.

30 V. Zila, E. Margiotta, B. Turoňová, T. G. Müller, C. E. Zimmerli, S. Mattei, M. Allegretti, K. Börner, J. Rada, B. Müller, M. Lusic, H.-G. Kräusslich and M. Beck, *Cell*, 2021, **184**, 1032–1046.e18.

31 H. Zhao, F. Liang, X. Qu, Q. Wang and Z. Yang, *Macromolecules*, 2015, **48**, 700–706.

32 J. A. Finbloom, C. Huynh, X. Huang and T. A. Desai, *N at. Rev. Bioeng.*, 2023, **1**, 139–152.

33 S. J. Goodband, S. Armstrong, H. Kusumaatmaja and K. Voitchovsky, *Langmuir*, 2020, **36**, 3461–3470.

34 B. V. Orme, G. McHale, R. Ledesma-Aguilar and G. G. Wells, *Langmuir*, 2019, **35**, 9146–9151.

35 J. D. Smith, R. Dhiman, S. Anand, E. Reza-Garduno, R. E. Cohen, G. H. McKinley and K. K. Varanasi, *Soft Matter*, 2013, **9**, 1772–1780.

36 T.-S. Wong, S. H. Kang, S. K. Y. Tang, E. J. Smythe, B. D. Hatton, A. Grinthal and J. Aizenberg, *Nature*, 2011, **477**, 443–447.

37 B. J. Connolly, E. Loth and C. F. Smith, *Powder Technol.*, 2020, **363**, 275–285.

38 S. Zhou, Y. Yang and H. Shang, *Processes*, 2024, **12**, 735.

39 P. Zhang, H. Chen, L. Zhang, T. Ran and D. Zhang, *Appl. Surf. Sci.*, 2015, **355**, 1083–1090.

40 A. K. Epstein, T.-S. Wong, R. A. Belisle, E. M. Boggs and J. Aizenberg, *Proc. Natl. Acad. Sci. U. S. A.*, 2012, **109**, 13182–13187.

41 G. Wang and Z. Guo, *Nanoscale*, 2019, **11**, 22615–22635.

42 K. A. Brakke, *Exp. Math.*, 1992, **1**, 141–165.

43 C. A. Schneider, W. S. Rasband and K. W. Eliceiri, *Nat. Methods*, 2012, **9**, 671–675.

44 H.-J. Butt and M. Jaschke, *Nanotechnology*, 1995, **6**, 1.

45 F. Bresme and M. Oettel, *J. Phys.: Condens. Matter*, 2007, **19**, 413101.

46 B. M. Law, S. P. McBride, J. Y. Wang, H. S. Wi, G. Paneru, S. Betelu, B. Ushijima, Y. Takata, B. Flanders, F. Bresme, H. Matsubara, T. Takiue and M. Aratono, *Prog. Surf. Sci.*, 2017, **92**, 1–39.

47 A. Amirfazli and A. W. Neumann, *Adv. Colloid Interface Sci.*, 2004, **110**, 121–141.

48 S. Friedrich and B. Cappella, *Tribol. Lett.*, 2020, **68**, 36.

49 P. Boonpuek and J. R. Felts, *Beilstein J. Nanotechnol.*, 2023, **14**, 1200–1207.

50 Y. D. Yan, T. Sun and S. Dong, *Wear*, 2007, **262**, 477–483.

51 J. W. Gibbs, *Am. J. Sci.*, 1878, **s3–16**, 441–458.

52 C. Fong, *arXiv*, 2021, preprint, arXiv:1604.02174, DOI: **10.48550/arXiv.1604.02174**.

53 *Bruker, Sharp Nitride Lever Probes | Contact Mode | Bruker AFM Probes*, **https://www.brukerafmprobes.com/p-3693-snl-10.aspx?srsltid=AfmBOoolX-oStt1Uy_jf_0DAuG8ZMF1D-SSeWLlM6Wm-OLHxrT5wKXSF**, (accessed August 31, 2024).

54 J. Ally, M. Kappl and H.-J. Butt, *Langmuir*, 2012, **28**, 11042–11047.

55 K. Kobayashi, J. Wei, R. Iida, K. Ijiro and K. Niikura, *Polym. J.*, 2014, **46**, 460–468.

56 G. T. Nguyen, E. L. Chan, T. Tsuji, T. Tanaka and K. Washino, *Adv. Powder Technol.*, 2021, **32**, 1410–1425.

57 K. W. Connington, T. Lee and J. F. Morris, *J. Comput. Phys.*, 2015, **283**, 453–477.

58 T. Krüger, H. Kusumaatmaja, A. Kuzmin, O. Shardt, G. Silva and E. M. Viggen, *The Lattice Boltzmann Method*, Springer Cham, 1st edn, 2016.